Research Article Vol. 32, No. 17 / 12 Aug 2024 / Optics Express 29174

Optics EXPRESS

# All-dielectric ultra-broadband transparent imidazole ionic liquid-based metamaterial absorber with a frustum-shaped structure

YONGJI GUAN, JIAJUN FAN, YUYANG WANG, XIAOXIANG LI, AND XIAOPING ZHANG*

*Institute of Optoelectronics and Electromagnetic Information, School of Information Science and Engineering, Lanzhou University, Lanzhou 730000, China*

*zxp@lzu.edu.cn

**Abstract:** In this study, a frustum-shaped addition was made to a cylindrical absorber unit, utilizing 1-ethyl-3-methylimidazolium dicyanamide ionic liquid (IL) to create a transparent all-dielectric liquid metamaterial absorber (A-D ILMMA). The A-D ILMMA achieved over 90% absorption efficiency across 4.86–50.00 GHz, with a 165% relative absorption bandwidth. It maintained robust performance across various polarization angles and achieved over 77% absorption at incident angles of up to 60°. Owing to the excellent thermal stability of the IL, the A-D ILMMA consistently maintained an absorption rate of over 90% across a temperature range from 25 °C to 100 °C. The high absorption rates were attributed to synergistic impedance matching and electromagnetic energy loss. The experimental results confirmed over 90% absorption in the ultra-broadband range of 7.10 GHz to 40.00 GHz, demonstrating the excellent physicochemical properties of ILs and their potential applications.



## 1. Introduction

Metamaterials are artificial periodic structures that can change the dielectric constant and permeability by changing the array structure to obtain specific electromagnetic (EM) properties that are not easily obtained in nature [1,2]. They have been widely used in EM energy harvesting [3–5], stealth technology [6–8], sensing [9,10] and other fields [11–13]. In particular, metamaterials can be used to build perfect absorbers that fully absorb certain frequencies of EM waves [14,15]. The first metamaterial absorber (MMA) was proposed by Landy *et al.* in 2008 [16]. Since then, MMA has received a lot of attention owing to its superior ability to absorb EM waves [14,17]. Most MMAs of this type have a three-layer configuration consisting of a dielectric spacer layer and two separate metal layers [18–20]. The three-layer structure concentrates the incident EM waves between the two metal layers, dissipating them into heat at the resonant frequency of the MMA [21]. Its design is simple, and the absorption of EM waves mainly depends on strong EM resonance; however, the absorption bandwidth is narrow [22]. There are several ways to expand the absorption bandwidth of MMAs [23–25], this can also lead to increased thickness and manufacturing difficulties. These limitations can be overcome by replacing the metallic structure with dielectric one.

Dielectric MMAs can generate electric or magnetic resonance under the condition of complete resonant absorption, which can expand the absorption bandwidth. However, most dielectric MMAs proposed so far still use metallic ground to achieve full EM shielding, which inevitably generates problems such as EM interference. In addition, metal has defects that are prone to corrosion and oxidation, which is another factor that limits its practical application. In recent years, all-dielectric MMAs (A-D MMAs) have been developed rapidly and have a wider range of applications. A-D MMAs usually consist of dielectric elements with high permittivity. Because of the high dielectric loss and obvious dielectric dispersion of water, water is widely used as

#530613 https://doi.org/10.1364/OE.530613
Journal © 2024 Received 20 May 2024; revised 16 Jul 2024; accepted 17 Jul 2024; published 29 Jul 2024

Optics EXPRESS

a medium in the design of A-D MMAs, and as a good solvent for ions, such as NaCl, is also added to water to obtain better absorption [26–32]. Wang *et al.* [28] proposed a water-based A-D MMA with over 90% absorption at 10.45–11.20 GHz with a relative bandwidth of 6.9%. Huang *et al.* [26] proposed a water-injected A-D MMA that achieves more than 90% absorption in the 8.10–22.90 GHz range. Xie *et al.* [27] proposed a water-based A-D MMA with highly uniform perfect absorption for frequencies between 7.74 GHz and 23.56 GHz and perfect thermal stability for temperatures from 0 °C to 100 °C. Lu *et al.* [30] proposed a transparent water-based A-D MMA that achieves more than 90% absorption in the 7.28 GHz–28.22 GHz range with a height of 6.9 mm. Li *et al.* [32] proposed a transparent water-based broadband A-D MMA based on laser cutting with more than 90% absorption in the range of 13.30 GHz to 40.00 GHz with a relative bandwidth of 100% and a height of 15.0 mm. Cao *et al.* [31] proposed a bi-directional water-based A-D MMA, which has an absorption rate of more than 90% in the range of 5.70 GHz to 41.60 GHz with a relative bandwidth of 152% at a height of 13.2 mm. Although water-based A-D MMAs have made great progress, water has poor thermal stability and easy evaporation/condensation. As an ideal alternative, ionic liquids (ILs) can be used as new liquid materials for liquid-based MMA.

ILs are a novel class of multifunctional solvents and soft materials, which are fused organic salts composed entirely of cations and anions with nearly infinite structural variations. Their properties can be significantly altered by adjusting their ionic combinations [33–35]. In 2019, Yang *et al.* [36] in our group first applied IL 1-ethyl-3-methylimidazolium tetrafluoroborate ([Emim][$BF_4$]) in the design of A-D MMAs, which has high EM loss characteristics and a wide liquid temperature range (-40–300°C) [37,38], and achieved absorption of microwaves above 90% in the 13.90–50.00 GHz range with a relative bandwidth of 113%. To enhance the impedance matching and economize on IL usage, in this study, we propose an all-dielectric ultra-broadband transparent MMA based on the IL 1-ethyl-3-methyl-imidazolium dicyanamide ([Emim][$N(CN)_2$]) with a frustum-shaped structure (A-D ILMMA). The simulation and experimental results show that when the total height is 17.0 mm, the absorptivity of the A-D ILMMA can exceed 90% in the range of 4.86–50.00 GHz, and the relative bandwidth is 165%. For polarization insensitivity, the absorptivity of the absorber remains unchanged as the polarization varies from 0° to 90°. For oblique incidence stability, in the TE mode, the absorptivity is more than 90% as the incident angle increases from 0° to 40°, and in the TM mode, the absorptivity is more than 90% as the incident angle increases from 0° to 60°. Furthermore, for thermal stability, the absorptivity of the absorber varies slightly from 25 °C to 100 °C. In addition, the ultra-broadband absorption mechanism of the absorber was studied. The excellent impedance matching performance of the designed structure and the high absorption performance of the IL [Emim][$N(CN)_2$] are key factors for the ultra-broadband absorption of the A-D ILMMA.

## 2. Design and simulation

The simulation of the metamaterial absorber was conducted using EM simulation software CST Microwave Studio over a frequency range of 0–50.00 GHz. The periodic cell structure was extended in the $x$ and $y$ directions. Floquet-port boundary conditions were applied on the $x$ and $y$ directional boundaries, with open (add space) boundary conditions in the $z$ direction to simulate infinite periodic structures. The incident wave was set as a uniform plane wave, the polarization direction was parallel to the $y$ axis, and the propagation direction was negative along the $z$ axis. The dielectric constant of the photosensitive resin is 3 and the tangent loss is 0.02. The EM absorptivity is defined as $A(\omega) = 1 - R(\omega) - T(\omega)$, the reflectivity is defined as $R(\omega) = |S_{11}(\omega)|^2$, and the transmissivity is $T(\omega) = |S_{21}(\omega)|^2$, where $\omega$ is the frequency of the incident EM wave.

The basic design process is illustrated in Fig. 1. All three models have the same IL layer height of 13.0 mm and unit cell width of 30.0 mm. Moreover, their resin side walls and bottom resin layers are 1.0 mm thick. Model_I is a simple model in which the IL is surrounded by an external

Optics EXPRESS

cylindrical resin layer. It is also the first MMA model based on the IL [39], although the previous model has different parameter values and metallic ground. In this case, only a small frequency range had an EM absorption rate greater than 90%. Compared with Model_I, a top dielectric layer (3.0 mm) was added to Model_II to build a multi-layer absorbing structure and optimize the impedance characteristics, so that the EM wave can be effectively absorbed [40]. However, the absorptivity of Model_II in the 20.00–30.00 GHz frequency range falls short of the desired goal. In the simulation process, we noticed that the part with a high power loss density was mainly concentrated at the junction between the IL and the resin layer in the upper part of the unit cell. Therefore, as shown in Model_III, an additional frustum was attached to the original resin cover, which also reduced the amount of the IL. Figure 1(b) clearly shows that the design of Model_III achieves a better absorption performance, reaching more than 90% absorptivity in the frequency range of 4.86 GHz to 50.00 GHz, corresponding to a relative bandwidth of 165%.

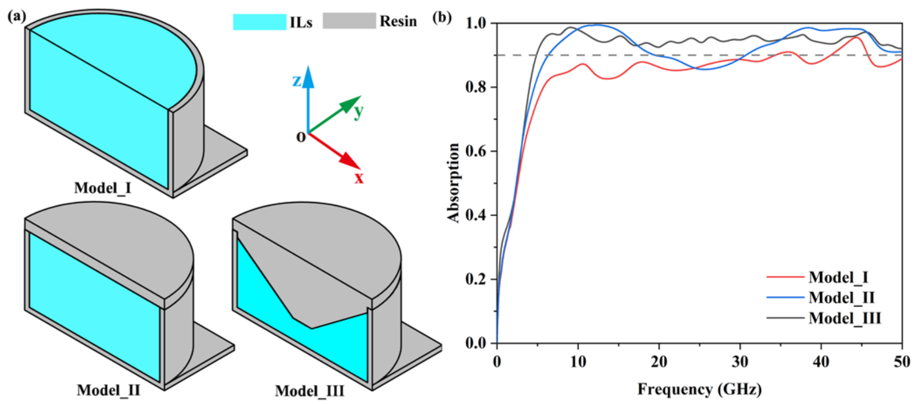


**Fig. 1.** (a) Cross-sectional view of designed unit cells named Model_I, Model_II and Model_III, respectively. (b) The simulated absorption spectrum of the designed structures from Model_I to Model_III.

Figure 2 shows the unit structure of absorber Model_III, including a bottom resin layer, cylindrical resin shell, internal IL layer and resin cover composed of a cylinder and frustum. The height of each section was determined using the combination of $h_1 - h_5$, as shown in Fig. 2(a). Simultaneously, as shown in Fig. 2(b), the lower surface radius of the top resin cover and the inner and outer radius of the resin shell are $r_1$, $r_2$ and $r_3$, respectively, and the period of the unit cell array is p. In order to find the optimal parameter combination, it is necessary to optimize the structure. By fixing the thickness of the bottom and side resin layers at 1.0 mm, scanning parameters p, $r_1$, $h_2$–$h_5$, changing the parameters in the model, and analyzing the impact of these changes on the absorption performance. The relationship between some important geometric parameters and the absorption rate is shown in Fig. 3. Firstly, $h_3 = 9.0$ mm, $h_5 = 2.0$ mm and $r_1 = 2.0$ mm is kept constant and $h_2$ is varied to observe its effect. Figure 3(a) shows that as the height of the lower IL layer $h_2$ increases, the absorption curve moves toward lower frequencies. Then, $h_2 = 4.0$ mm and $r_1 = 2.0$ mm are fixed and $h_3$ and $h_5$ are changed. Their performances in Fig. 3(b) and 3(c) are similar to that in Fig. 3(a). Finally, let $h_2$, $h_3$ and $h_5$ be 4.0, 9.0 and 2.0 mm, respectively, and change $r_1$. In Fig. 3(d), a slight change in $r_1$ of the resin cover has little effect on the overall absorption performance, and the absorption effect is best when $r_1 = 2.0$ mm. In general, within a certain range, the higher the height, the better is the absorption performance of the A-D ILMMA. After comprehensively considering the thickness and performance of the absorber, the present parameter values were selected. In the case of a comprehensive consideration of design and manufacturing, the size of the absorber unit structure is shown in Table 1, and its total thickness is 17.0 mm.

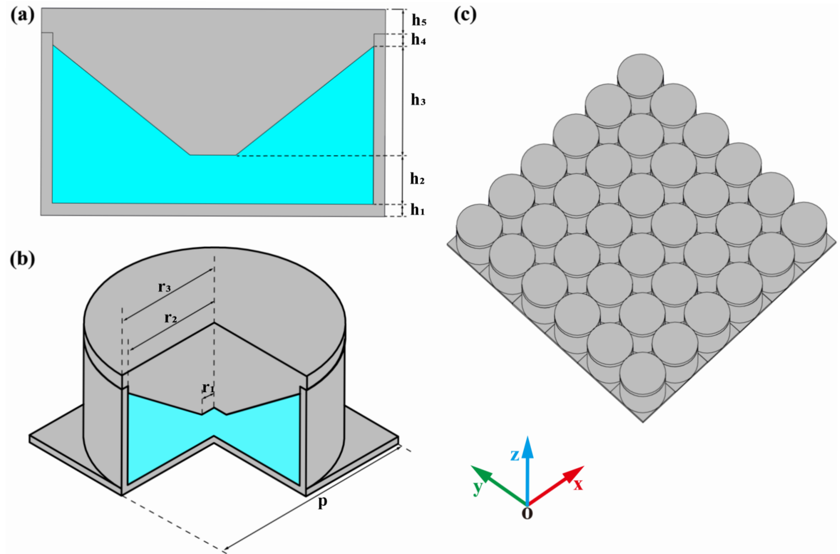


**Fig. 2.** The 3D schematic diagram of the A-D ILMMA. (a) Central cut plane view, (b) quarter cross-sectional view of the A-D ILMMA and (c) the top view of the A-D ILMMA.

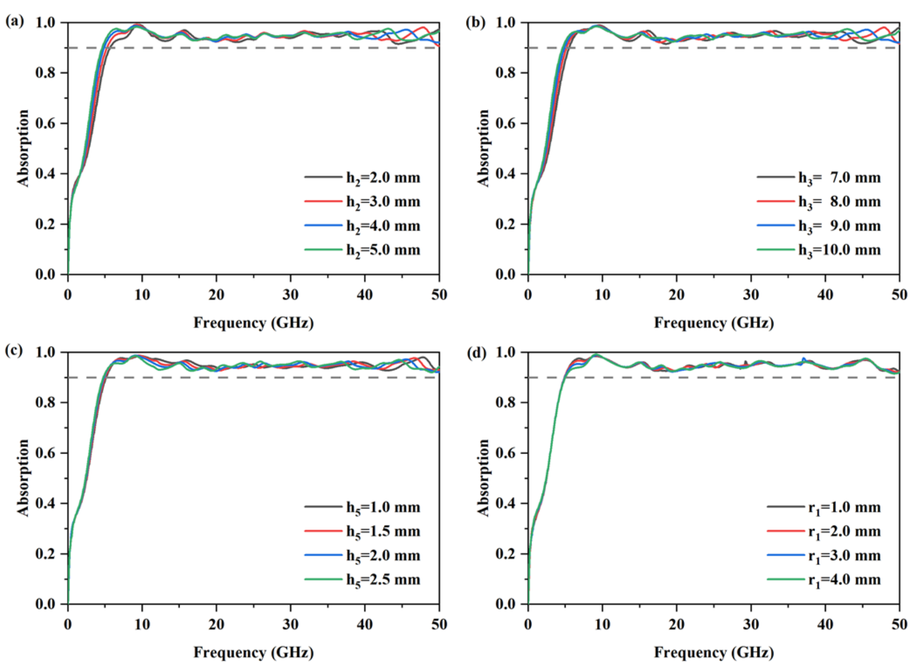


**Fig. 3.** Effect of changing geometric parameters, including (a) $h_2$, (b) $h_3$, (c) $h_5$, and (d) $r_1$. One parameter changes with others keep unchanged.

**Table 1. Geometric parameters of the A-D ILMMA**

| List | Geometric parameters | | | | |
|---|---|---|---|---|---|
| Parameters | $h_1$ | $h_2$ | $h_3$ | $h_4$ | $h_5$ |
| Value(mm) | 1.0 | 4.0 | 9.0 | 1.0 | 2.0 |
| Parameters | $r_1$ | $r_2$ | $r_3$ | p | ... |
| Value(mm) | 2.0 | 14.0 | 15.0 | 30.0 | ... |

For ILs, their dielectric constant can be expressed in complex form, with the real part representing their ability to store electrical energy, and the imaginary part reflecting their loss characteristics. The ratio of the imaginary part to the real part is called the loss tangent. A larger loss tangent value usually results in better absorption effects, while impedance matching should also be considered. Figure 4(a) shows the complex dielectric constants of four different ILs, and their corresponding absorption effects are illustrated in Fig. 4(b). The comparison reveals that [Emim][N(CN)$_2$] has the highest loss tangent value, leading to the best absorption effect. Therefore, it will be selected as the specific IL for subsequent simulation and experiment.

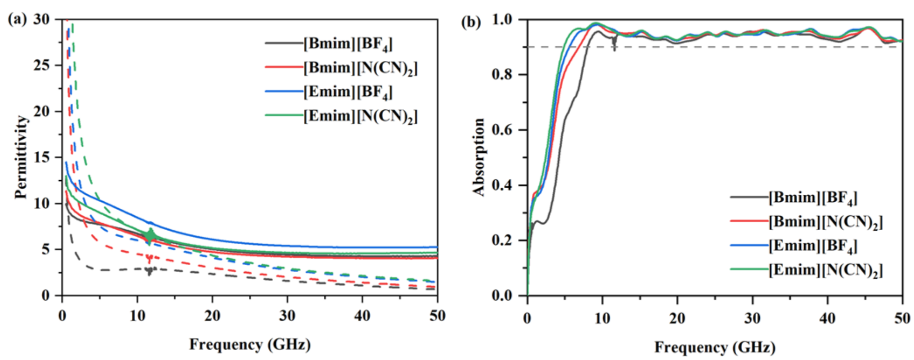


**Fig. 4.** (a) The real and imaginary parts of permittivity of four different ILs. The solid and dashed line represent the real and imaginary part, respectively. (b) The corresponding simulated absorption spectrum.

The normalized impedance of the designed A-D ILMMA can be calculated using the *S* parameters obtained by the simulation [41].

$$Z = \sqrt{\frac{(1+S_{11})^2 - S_{21}^2}{(1-S_{11})^2 - S_{21}^2}} \quad (1)$$

As depicted in Fig. 5(a), the normalized impedance is close to 1, which means that the A-D ILMMA has good impedance matching and EM wave absorption performance. In addition, the normalized power loss in Fig. 5(b) shows the contribution of the resin and IL to ultra-broadband absorption. Energy loss in the IL always dominates, but as the frequency increases, the gap between the two narrows gradually.

The absorption performance of the A-D ILMMA under TE and TM wave incidence and different polarization angles $\varphi$ and incident angles $\theta$ was further investigated, as shown in Fig. 6. As can be seen from Fig. 6(a) and 6(b), whether it is a TE or TM wave incident, the change in the polarization angle $\varphi$ has little effect on the absorption performance of the absorber. However, for different incident angles $\theta$, the performances of the TE wave and TM wave incidence differ significantly, as can be observed in Fig. 6(c) and 6(d). In the TE mode, the absorptivity was more than 90% as the incident angle increased from 0° to 40°, and in the TM mode, the absorptivity

Optics EXPRESS

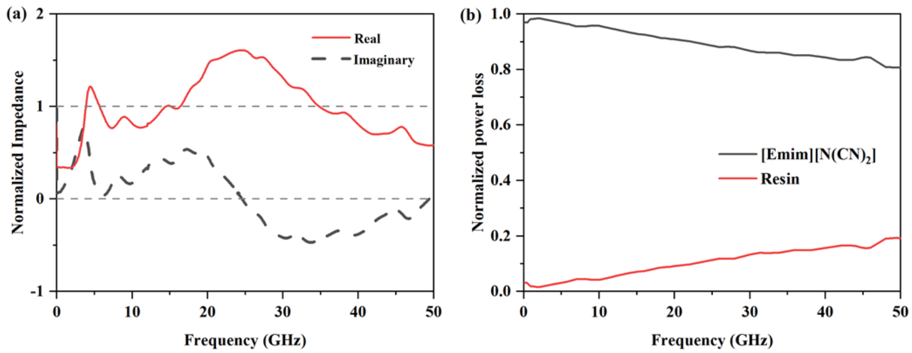


**Fig. 5.** (a) The calculated normalized impedance and (b) power loss of the A-D ILMMA.

was more than 90% as the incident angle increased from 0° to 60°. This phenomenon has been widely observed [42,43]. It was found that the variation in reflected waves at different interfaces is the cause of different behaviours [44]. For the TE mode, an increase in the incident angle widened the value difference between the waves reflected directly from the top interface and higher-order reflected waves. In other words, more EM waves are reflected and less EM energy is consumed by the absorber. Finally, when the incident angle is large, the absorption of the TE mode to EM wave attenuates. However, the TM mode exhibited a different mechanism. Owing to the combined effect of interference cancellation and intrinsic loss, EM wave absorbers with appropriate thickness can achieve effective absorption at large incident angles.

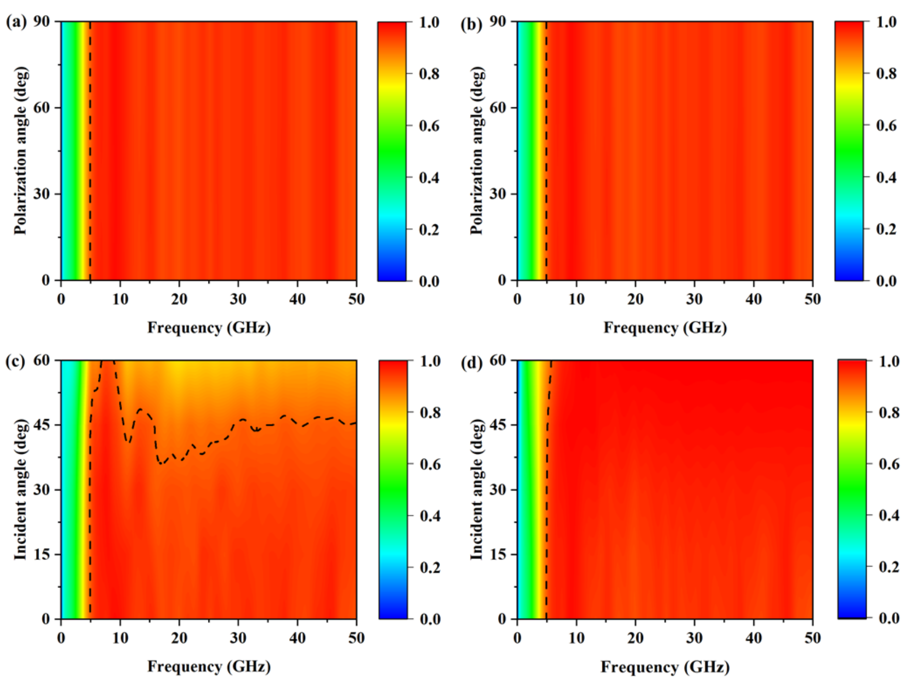


**Fig. 6.** The simulated results of the A-D ILMMA under (a) the oblique TE incidence with different polarization angle $\varphi$, (b) the oblique TM incidence with different polarization angle $\varphi$, (c) the oblique TE incidence with different incident angle $\theta$, (d) the oblique TM incidence with different incident angle $\theta$. The dashed line indicates 90% absorption.

The dielectric properties of the IL are affected by temperature, as shown in Fig. 7(a). Figure 7(b) shows the absorption performance of the A-D ILMMA from 25°C to 100 °C. With an increase in temperature, the absorption performance of the A-D ILMMA is almost unaffected, which indicates that the A-D ILMMA has good thermal stability.

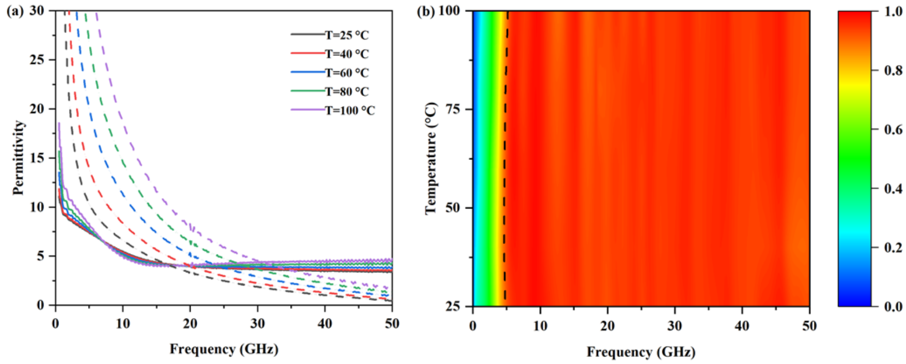


**Fig. 7.** The thermal absorption property of the A-D ILMMA. (a) The real part and imaginary part of permittivity for [Emim][N(CN)$_2$] at different temperatures from 25 °C to 100 °C. The solid and dashed line represent the real and imaginary part, respectively. (b)The simulated absorption spectrum of the A-D ILMMA under normal incidence with variable temperatures from 25 °C to 100 °C, and the dashed line indicates 90% absorption.

## 3. Ultra-broadband characteristics analysis

To elucidate the physical mechanism underlying the ultra-broadband absorption of the A-D ILMMA, an analysis of the electric and magnetic field distributions at the peak absorption frequencies was conducted. The absorption spectrum revealed resonances at frequencies 6.80 GHz, 9.15 GHz, 15.15 GHz, 18.40 GHz, 26.60 GHz, 31.75 GHz, 37.60 GHz, and 45.45 GHz, labeled as f1–f8. Figure 9(a) and 9(b) show the electric and magnetic field distributions, respectively. Figure 10(a)–(c) show the power loss density distribution at *yoz* cross section, at *xoz* cross-section and diagonal cross-section of the unit cell, respectively.

Power loss density is defined as [45]

$$P_{\text{loss}} = \frac{1}{2}\omega\varepsilon''|\vec{E}(\omega)|^2 \tag{2}$$

where $\varepsilon''$ is the imaginary part of the complex permittivity and $\vec{E}(\omega)$ is the electric field component of the EM wave at the corresponding frequency $\omega$. It can be observed that the normal component of the electric displacement vector $\vec{D}$ is continuous in the vertical direction of the boundary. According to the boundary condition formula for the electric displacement vector [46,47]

$$\vec{e}_n(\vec{D}_{\text{resin}} - \vec{D}_{\text{IL}}) = 0 \tag{3}$$

where $e_n$ is the normal vector of the surface, and the electric displacement vector $\vec{D}$ can be expressed as

$$\vec{D} = \varepsilon'\vec{E} \tag{4}$$

where $\varepsilon'$ is the real part of the complex permittivity. Because the real part of the complex permittivity of the resin is relatively smaller than that of the IL, the electric field intensity in the resin shell is relatively stronger, which is consistent with Fig. 9, and the electric field vector ring is concentrated at the junction between the IL and resin shell. However, because $\varepsilon''_{\text{resin}} \ll \varepsilon''_{\text{IL}}$, the power loss density in the IL is larger than that in the resin. Simultaneously, EM waves are attenuated when propagating in the IL layer. Therefore, according to Eq. (2), the power loss density is mainly concentrated in IL, and the power loss density at the IL boundary is dominant. This reveals the reason for the better absorption effect of the proposed A-D ILMMA. Compared to IL, resin has a smaller real part of dielectric constant, making it easier to achieve impedance matching with free space. Replacing part of the IL with a frustum-shaped resin structure can further optimize impedance matching, allowing EM waves to enter the absorber as much as possible without reflection, and instead be consumed by the IL.

To further illustrate the difference between the optimized structure and the other structures, the power loss density distribution of the three models in Fig. 1 at different frequencies were simulated. The selected frequencies are 9.15 GHz, 18.40 GHz, 31.75 GHz and 45.45 GHz, which correspond to f2, f4, f6 and f8 of the peak frequencies mentioned before, as shown in Fig. 8. Because the EM wave loss mainly occurs in the IL, only part of the IL layer is intercepted here for convenience of observation. For all three models, the EM wave loss is primarily distributed at the top. Comparing the situation of Model_I and Model_II, it can be seen that the top of the IL layer of Model_II shows more obvious EM wave energy loss characteristics, because the added resin cover improves the impedance matching performance between the absorber and air. For the optimized structure, Model_III, as shown in Fig. 8(c), the power loss at different frequencies is stronger than that of Model_I and Model_II, which indicates that the A-D ILMMA can further improve the impedance matching, so that more EM waves can enter the absorber, more precisely the IL layer, and be absorbed more efficiently by the IL. Therefore, the A-D ILMMA exhibited a strong EM wave absorption capability over a wider frequency range.

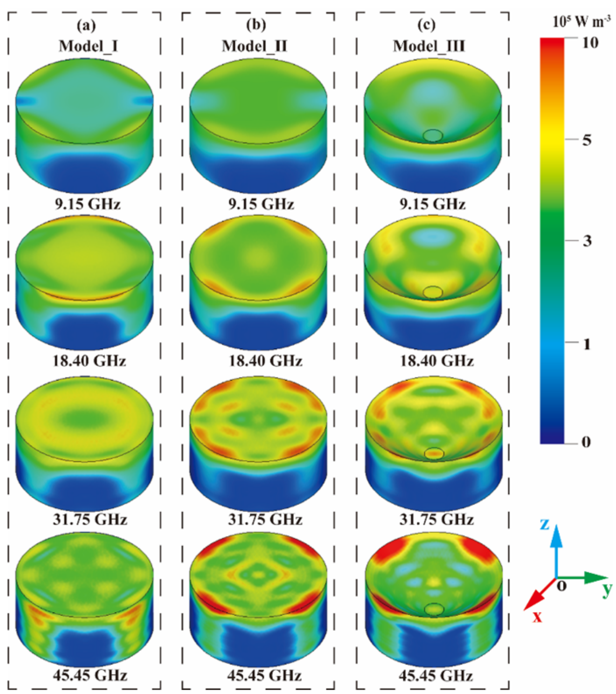


**Fig. 8.** The distributions of power loss density at different frequencies for three different absorber structures (a) Model_I, (b) Model_II and (c) Model_III.

A detailed field distribution analysis of the A-D ILMMA was then carried out. For the first resonance of f1 = 6.80 GHz, field analysis shows that the electric field is mainly concentrated in

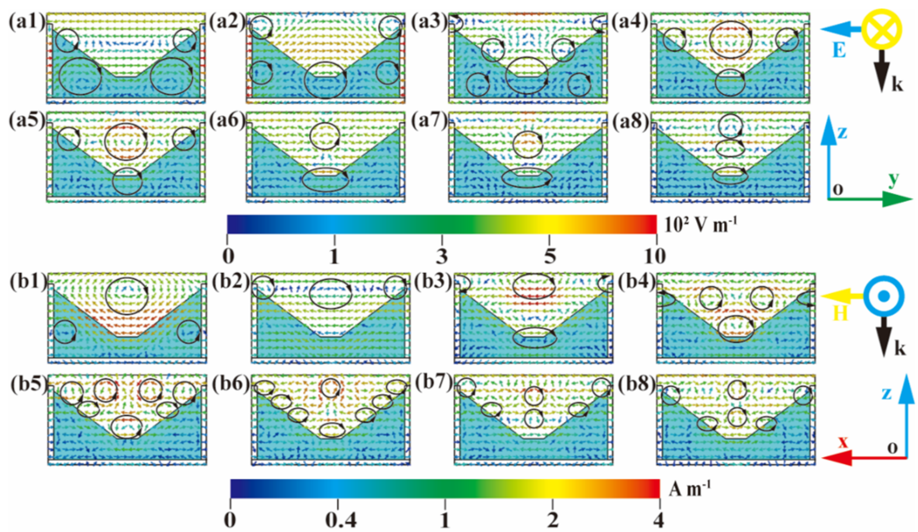


**Fig. 9.** Simulated field analysis of the A-D ILMMA. (a1–a8) The electric vector field distributions, (b1–b8) the magnetic vector field distributions under normal incidence at frequencies f1–f8, respectively.

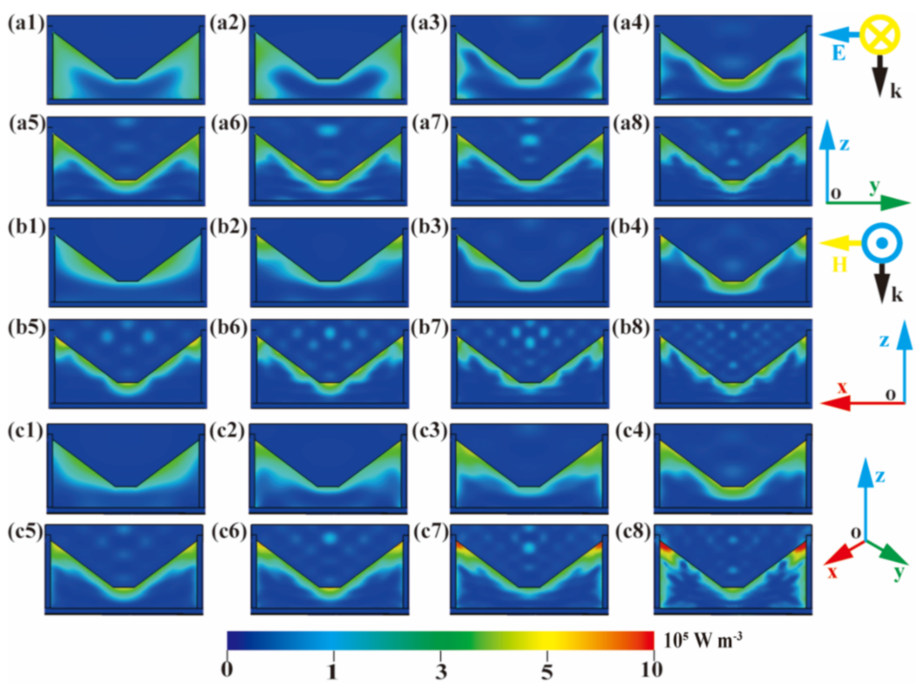


**Fig. 10.** The power loss density distributions of the A-D ILMMA (a1–a8) at *yoz* cross-section, (b1–b8) at *xoz* cross-section, (c1–c8) at diagonal cross-section of the unit cell under normal incidence at frequencies f1–f8, respectively.

the resin cover and cylindrical resin shell. The electric field produces two clockwise vector rings in the IL layer, and two anticlockwise vector rings at the junction between the resin cover and IL

Optics EXPRESS

layer; thus, the unit cell is equivalent to two pairs of magnetic dipoles with the same polarization direction, forming a strong magnetic resonance. The magnetic field is mainly concentrated at the junction between the lower part of the resin cover and the IL layer, and two anticlockwise vector rings are also generated in the IL layer, which is equivalent to two electric dipoles with the same polarization direction and produces electric resonance. Under the combined effect of magnetic and electric resonance, energy loss is mainly distributed at the junction between the dielectric cover and IL layer and at the junction between the side wall and IL layer.

At f2 = 9.15 GHz, the electric field generated two clockwise vector rings in the IL layer, two anticlockwise vector rings at the junction between the resin cover and IL layer, and one clockwise vector ring at the junction between the lower part of the resin cover and IL layer, thus forming a strong magnetic resonance. The magnetic field generates one clockwise vector ring in the resin cover, and two clockwise vector rings are also generated in the IL layer, which is equivalent to two electric dipoles with the same polarization direction, generating an electric resonance. Similar to f1, the energy loss is mainly distributed in the resin cover and the junction between the side wall and the IL layer. Although electric resonance also exists in the dielectric cover, there is no significant energy loss in the resin cover because the dielectric constant of the IL [Emim][N$(CN)_2$] is much larger than that of the resin.

The situation at f3 is similar to that of f2, but annular electric and magnetic field distributions also appear between neighboring cells in addition to the interior of the cell. Owing to the close distance between adjacent cells, a strong coupling effect is generated, resulting in magnetic and electric resonance. For f4–f8, the electric field produces multiple vector rings at the interface between the resin cover and IL layer, forming magnetic resonance. The magnetic field also produces multiple vector rings at the interface between the resin cover and the IL layer, forming magnetic resonance. Energy loss is mainly distributed at the junction between the cover and IL layer, which exhibits properties similar to interface polarization, although the interface polarization reported so far is at the semiconductor-semiconductor interface [48,49].

It should be pointed out that, as shown in Fig. 10(c), there is also a large power loss density at the diagonal cross-section of the unit cell. In particular, when the incident frequency is greater

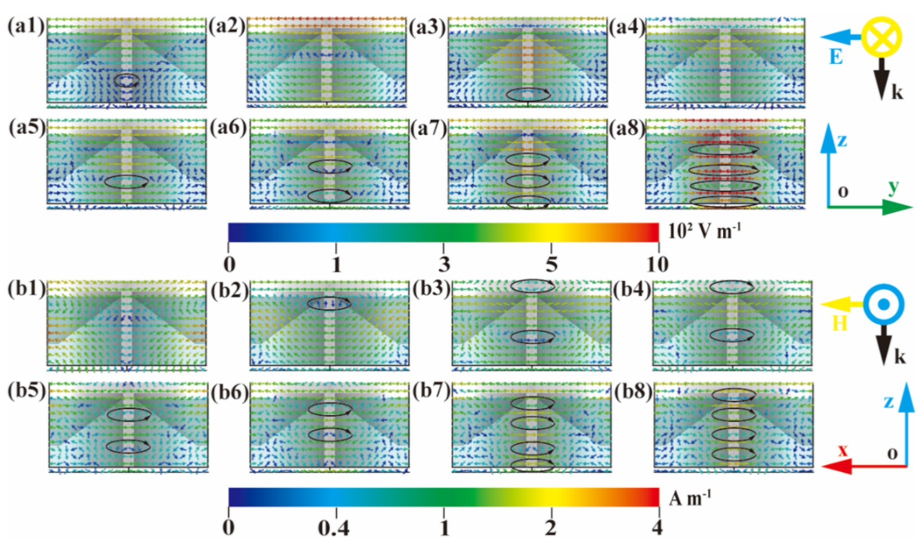


**Fig. 11.** Simulated field analysis at the junction of unit cells. (a1–a8) The electric vector field distributions, (b1–b8) the magnetic vector field distributions under normal incidence at frequencies f1–f8, respectively.

than 37.60 GHz, the power loss density at this cross-section is dominant. The reason for this phenomenon is that the dielectric loss material will produce conductivity, polarization, thermal effects and other phenomena under the action of the EM field, so that the energy of the EM wave is partially converted into heat energy and lost. In this way, the EM field in the medium will be weaker than the EM field in the vacuum, the EM field in the vacuum around the unit cell is relatively large, and its center is located in the $z$ axis direction of the four corners of the unit cell, so that the power loss density distribution at the diagonal cross-section becomes larger. Figure 11 shows the electric and magnetic field distributions at the junction of adjacent unit cells, with half of each of the two cells shown. For f7 and f8, the electric and magnetic fields in vacuum are larger than those in the absorber. The electric field forms multiple closed vector rings at the unit cell junction, and the adjacent electric field vector rings have opposite directions, and still exhibits the magnetic resonance effect of magnetic dipoles after superposition. The situation in magnetic fields is similar to that in electric fields. This explains the anomalous situation shown in Fig. 10(c). After analyzing the electric and magnetic field distributions of the A-D ILMMA, it is clear that the EM energy loss originates from two sources: ohmic loss due to electric resonance and dielectric loss due to magnetic resonance, which are then converted to heat energy. In general, there are hybrid composite resonance modes at all eight peak frequencies, which contribute to broadband absorption from 4.86 GHz to 50.00 GHz.

## 4. Experimental results and discussion

To ensure the accuracy of the simulation analysis, it was necessary to test the absorption effect of the A-D ILMMA. The measurement of the reflection coefficient and transmission coefficient was realized by the free-space method in the microwave anechoic chamber. As shown in Fig. 12(a), the test system is mainly composed of a Vector Network Analyzer (Ceyear AV3672E), computer, horn antennas, coaxial lines, etc., which can measure the reflection coefficient of the absorbing material. The test methods for the transmission coefficient and reflection coefficient of the absorber are different, and cannot be completed at the same time; therefore, the test device needs to be adjusted, as shown in Fig. 12(b). The transmitting antenna was placed above the test sample and the receiving antenna was placed directly below the test sample. According to the different operating frequencies, the horn antenna is divided into three specifications: 2.00–18.00 GHz, 18.00–26.50 GHz and 26.50–40.00 GHz. Before the test and after each change in the horn antennas, the test system was corrected using an aluminum plate.

The fabrication process of the A-D ILMMA was as follows. First, a photosensitive resin medium scaffold needs to be made according to the simulation size by 3D printing method. Then, 5.9 mL of IL [Emim][$N(CN)_2$] was injected into each cylindrical groove of the scaffold with a glue head dropper, and the final fabrication of the absorber was completed after the resin cover was covered. The dimensions of the experimental sample were 180.0 mm $\times$ 180.0 mm $\times$ 17.0 mm.

Using the above experimental setup, the reflection coefficient ($S_{11}$) and transmission coefficient ($S_{21}$) of the A-D ILMMA were tested, and the corresponding absorption rate was obtained using the formula $A(\omega) = 1 - |S_{11}(\omega)|^2 - |S_{21}(\omega)|^2$, as shown in Fig. 12(c). The test results showed that the absorber was more than 90% in the frequency range of 7.10–40.00 GHz. It was found that the upper stopband frequency in the simulation was 4.86 GHz, while the test result was 7.10 GHz. In the test range of 2.00–18.00 GHz for the first pair of horn antennas, the test absorption rate was slightly smaller than the simulated value. In the test range of 18.00 to 40.00 GHz for the other two pairs of antennas, the test absorption rate was comparable to the simulated value. The main reasons for these errors are as follows: First, when the reflection coefficient is tested, in order to avoid collision, the angle of the horn antennas cannot be zero, which is different from the simulation, leading to a change in the absorption curve. Second, the amount of IL was not sufficiently accurate, the actual height of the IL layer was slightly lower than the simulated

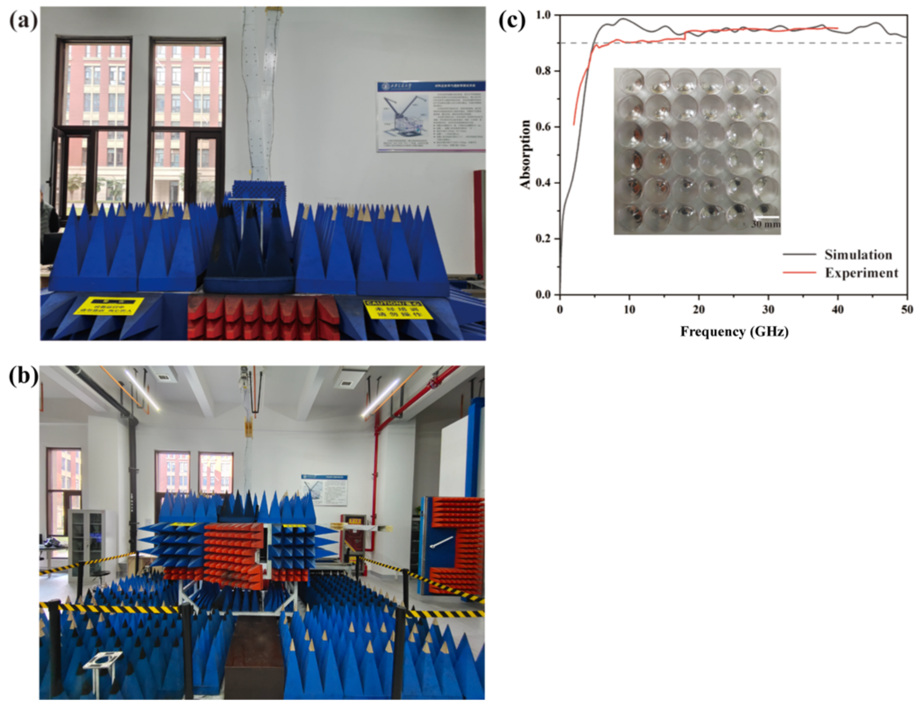


**Fig. 12.** (a) Photograph of the experimental setup for testing reflection coefficient and (b) transmission coefficient, (c) comparison of absorption spectra between simulation and experimental results.

height, and the absorption curve moved to a higher frequency. Third, because the test result is sensitive to the processing errors of the test samples, the errors generated in the process of manufacturing the resin scaffold using 3D printing technology are also factors that lead to the differences between the test result and the simulated value. Because of the lack of horn antennas with higher operating frequencies in the laboratory, it cannot be tested in the frequency range of 40.00–50.00 GHz. However, according to existing test data, the A-D ILMMA can realize broadband wave absorption in this frequency range, which verifies the correctness and reliability of the simulation results. Figure 13 shows a comparison of the simulation and experimental results of the A-D ILMMA under oblique TE incidence with different incident angles $\theta$. It can be seen that the absorption effect of the absorber gradually weakens as the incident angle $\theta$ increases, and the simulation results are consistent with the experimental results.

A comparative evaluation of the A-D ILMMA designed in this study and previously published IL-based A-D LMMAs was performed, focusing on the effective absorption frequency range and relative absorption bandwidth. As shown in Table 2, both the effective bandwidth and relative absorption bandwidth of the A-D ILMMA exceed the absorber bandwidth proposed in previous study. The superior ultra-broadband performance of the A-D ILMMA can be attributed to the excellent impedance matching performance and high EM loss characteristics of the IL [Emim][$N(CN)_2$]. The A-D ILMMA not only shows excellent absorption ability, but also verifies the feasibility of the optimized structure and the effectiveness of IL selection, which sets a new benchmark in the field of ultra-broadband A-D MMAs.

Research Article | Vol. 32, No. 17 / 12 Aug 2024 / Optics Express 29186


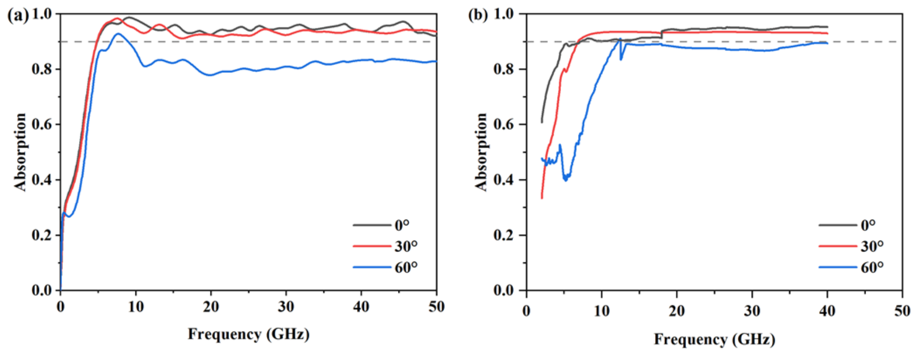


**Fig. 13.** (a) The simulated results and (b) the experimental results of the A-D ILMMA under the oblique TE incidence with different incident angle $\theta$.

**Table 2. Comparison with previous works**

| Ref. | RB (%) | BW (GHz) | Thickness(mm) | Transparent |
|---|---|---|---|---|
| [26] | 96 | 8.10–22.90 | 5.6 | No |
| [27] | 101 | 7.74–23.56 | 12.8 | No |
| [28] | 7 | 10.45–11.20 | 9.0 | Yes |
| [30] | 118 | 7.28–28.22 | 6.5 | Yes |
| [31] | 152 | 5.70–41.60 | 13.2 | Yes |
| [32] | 100 | 13.30–40.00 | 15.0 | Yes |
| This work | 165 | 4.86–50.00 | 17.0 | Yes |

## 5. Conclusions

In this study, the IL [Emim][N(CN)$_2$], with its high dielectric loss characteristics and wide liquid temperature range, was considered as a promising absorbing material. Subsequently, after the structural optimization of the cylindrical absorber cell structure, it was injected into the unit cell as a dielectric loss medium to construct the transparent A-D ILMMA. Numerical analysis shows that the proposed A-D ILMMA achieves an absorption rate of more than 90% over the 4.86–50.00 GHz spectrum, and a relative absorption bandwidth of 165%. Owing to its symmetric structural design, the A-D ILMMA exhibits polarization insensitivity and can maintain stable absorption properties over a wide polarization angle range from 0° to 90°. In addition, even if the incident angle increases to 60°, the A-D ILMMA can maintain an absorption rate of more than 77% in the frequency band of 4.86–50.00 GHz, which highlights its wide-angle absorption ability.

The temperature-dependent behaviour of the A-D ILMMA absorption was explored in detail. Specifically, as the temperature increases from 25 °C to 100 °C, the dielectric constant of the IL changed accordingly, but the absorption rate remained above 90%. The mechanism analysis shows that the ultra-broadband absorption ability of the proposed A-D ILMMA is a synergistic result of the excellent impedance matching performance and EM energy loss. The optimized structure greatly improves the impedance matching performance of the absorber, while the underlying mechanism of the observed EM energy loss can be traced back to dielectric and ohmic losses. These losses are converted into thermal energy, and this phenomenon is mainly driven by strong macroscopic magnetic and electric resonance. In particular, the power loss density distribution at the diagonal section of the A-D ILMMA was investigated, and it was found that the power loss in this section was dominant at high frequencies (> 37.60 GHz) owing to the influence of the external EM field.

The experimental evaluation confirmed the above findings, confirming the excellent EM wave absorption capability of the A-D ILMMA. The absorber consistently exhibited an absorption rate of over 90% in the ultra-broadband frequency range from 7.10 GHz to 40.00 GHz. This observation agrees with previous numerical predictions and further illustrates the robustness and potential applicability of the A-D ILMMA in relevant application domains.

**Funding.** Natural Science Foundation of Gansu Province (23JRRA1112); National Natural Science Foundation of China (62061025); Scientific Research Foundation of Lanzhou University for the Talented Young Scholars (561120207).

**Acknowledgements.** The authors acknowledge the financial support of this work from the Fund for Natural Science Foundation of Gansu Province for Young Scientists (23JRRA1112), Less Developed Regions of the National Natural Science Foundation of China (62061025) and the Scientific Research Foundation of Lanzhou University for the Talented Young Scholars (561120207).

**Disclosures.** The authors declare no conflicts of interest.

**Data availability.** Data underlying the results presented in this paper are not publicly available at this time but may be obtained from the authors upon reasonable request.

## References

1. W. J. Padilla, D. N. Basov, D. R. Smith, *et al.*, "Negative refractive index metamaterials," Mater. Today **9**(7-8), 28–35 (2006).
2. T. J. Cui, M. Q. Qi, X. Wan, *et al.*, "Coding metamaterials, digital metamaterials and programmable metamaterials," Light: Sci. Appl. **3**(10), e218 (2014).
3. M. Bakir, M. Karaaslan, F. Dincer, *et al.*, "Electromagnetic energy harvesting by using tunable metamaterial absorbers," in *23nd Signal Processing and Communications Applications Conference (SIU), Signal Processing and Communications Applications Conference* (2015), 467–469.
4. X. Duan, X. Chen, Y. Zhou, *et al.*, "Wideband metamaterial electromagnetic energy harvester with high capture efficiency and wide incident angle," Antennas Wirel. Propag. Lett. **17**(9), 1617–1621 (2018).
5. S. Ijaz, A. S. Rana, Z. Ahmad, *et al.*, "Exploiting zirconium nitride for an efficient heat-resistant absorber and emitter pair for solar thermophotovoltaic systems," Opt. Express **29**(20), 31537–31548 (2021).
6. J. B. Pendry, D. Schurig, D. R. Smith, *et al.*, "Controlling electromagnetic fields," Science **312**(5781), 1780–1782 (2006).
7. D. Schurig, J. J. Mock, B. J. Justice, *et al.*, "Metamaterial electromagnetic cloak at microwave frequencies," Science **314**(5801), 977–980 (2006).
8. H. H. Chen, W. Ma, Z. Huang, *et al.*, "Graphene-based materials toward microwave and terahertz absorbing stealth technologies," Adv. Opt. Mater. **7**(8), 1801318 (2019).
9. N. Liu, M. Mesch, T. Weiss, *et al.*, "Infrared perfect absorber and its application as plasmonic sensor," Nano Lett. **10**(7), 2342–2348 (2010).
10. Y. S. Zhang, P. Lin, Yu-Sheng Lin, *et al.*, "Tunable split-disk metamaterial absorber for sensing application," Nanomaterials **11**(3), 598 (2021).
11. F. Tofigh, M. Amiri, N. Shariati, *et al.*, "Polarization-insensitive metamaterial absorber for crowd estimation based on electromagnetic energy measurements," IEEE Trans. Antennas Propag. **68**(3), 1458–1467 (2020).
12. H. Y. Cai, Y. Sun, X. Wang, *et al.*, "Design of an ultra-broadband near-perfect bilayer grating metamaterial absorber based on genetic algorithm," Opt. Express **28**(10), 15347–15359 (2020).
13. S. Ijaz, A. Sarwar Rana, Z. Ahmad, *et al.*, "The dawn of metadevices: from contemporary designs to exotic applications," Advanced Devices & Instrumentation **2022**, 9861078 (2022).
14. C. M. Watts, X. Liu, W. J. Padilla, *et al.*, "Metamaterial electromagnetic wave absorbers," Adv. Mater. **24**(23), OP98–OP120 (2012).
15. P. Yu, L. V. Besteiro, Y. Huang, *et al.*, "Broadband metamaterial absorbers," Adv. Opt. Mater. **7**(3), 1800995 (2019).
16. N. I. Landy, S. Sajuyigbe, J. J. Mock, *et al.*, "Perfect metamaterial absorber," Phys. Rev. Lett. **100**(20), 207402 (2008).
17. X. J. Zeng, X. Cheng, R. Yu, *et al.*, "Electromagnetic microwave absorption theory and recent achievements in microwave absorbers," Carbon **168**, 606–623 (2020).
18. R. Yahiaoui, J. P. Guillet, Frédérick de Miollis, *et al.*, "Ultra-flexible multiband terahertz metamaterial absorber for conformal geometry applications," Opt. Lett. **38**(23), 4988–4990 (2013).
19. G. S. Deng, P. Chen, J. Yang, *et al.*, "Graphene-based tunable polarization sensitive terahertz metamaterial absorber," Opt. Commun. **380**, 101–107 (2016).
20. F. Chen, Y. Cheng, H. Luo, *et al.*, "Temperature tunable narrow-band terahertz metasurface absorber based on InSb micro-cylinder arrays for enhanced sensing application," IEEE Access **8**, 82981–82988 (2020).
21. W. D. Xu, L. Xie, Y. Ying, *et al.*, "Mechanisms and applications of terahertz metamaterial sensing: a review," Nanoscale **9**(37), 13864–13878 (2017).

22. P. Moitra, B. A. Slovick, Z. Gang Yu, *et al.*, "Experimental demonstration of a broadband all-dielectric metamaterial perfect reflector," Appl. Phys. Lett. **104**(17), 171102 (2014).
23. J. W. Park, P. Van Tuong, J. Y. Rhee, *et al.*, "Multi-band metamaterial absorber based on the arrangement of donut-type resonators," Opt. Express **21**(8), 9691–9702 (2013).
24. J. Grant, Y. Ma, S. Saha, *et al.*, "Polarization insensitive, broadband terahertz metamaterial absorber," Opt. Lett. **36**(17), 3476–3478 (2011).
25. H. K. Kim, D. Lee, S. Lim, *et al.*, "Frequency-tunable metamaterial absorber using a varactor-loaded fishnet-like resonator," Appl. Opt. **55**(15), 4113–4118 (2016).
26. X. Huang, H. Yang, Z. Shen, *et al.*, "Water-injected all-dielectric ultra-wideband and prominent oblique incidence metamaterial absorber in microwave regime," J. Phys. D: Appl. Phys. **50**(38), 385304 (2017).
27. J. Xie, S. Quader, F. Xiao, *et al.*, "Truly all-dielectric ultrabroadband metamaterial absorber: water-based and ground-free," Antennas Wirel. Propag. Lett. **18**(3), 536–540 (2019).
28. Q. M. Wang, K. Bi, S. Lim, *et al.*, "All-dielectric transparent metamaterial absorber with encapsulated water," IEEE Access **8**, 175998–176004 (2020).
29. F. Lan, Zi-Fan Meng, Jiu-Fu Ruan, *et al.*, "All-dielectric water-based metamaterial absorber in terahertz domain," Opt. Mater. **121**, 111572 (2021).
30. Y. Lu, J. Chen, J. Li, *et al.*, "Design of all-dielectric ultra-wideband transparent water-based absorber," J. Phys. D: Appl. Phys. **55**(11), 115502 (2022).
31. M. Cao, X. Huang, L. Gao, *et al.*, "Broadband bi-directional all-dielectric transparent metamaterial absorber," Nanomaterials **12**(23), 4124 (2022).
32. L. T. Li, J. Wen, Y. Wang, *et al.*, "A Transparent broadband all-dielectric water-based metamaterial absorber based on laser cutting," Phys. Scr. **98**(5), 055516 (2023).
33. N. V. Plechkova and K. R. Seddon, "Applications of ionic liquids in the chemical industry," Chem. Soc. Rev. **37**(1), 123–150 (2008).
34. M. J. A. Shiddiky and A. A. J. Torriero, "Application of ionic liquids in electrochemical sensing systems," Biosens. Bioelectron. **26**(5), 1775–1787 (2011).
35. S. G. Zhang, J. Zhang, Y. Zhang, *et al.*, "Nanoconfined ionic liquids," Chem. Rev. **117**(10), 6755–6833 (2017).
36. E. Yang, F. Yang, J. Pei, *et al.*, "All-dielectric ultra-broadband metamaterial absorber based on imidazole ionic liquids," J. Phys. D: Appl. Phys. **52**(39), 395501 (2019).
37. J. G. Huddleston, H. D. Willauer, R. P. Swatloski, *et al.*, "Room temperature ionic liquids as novel media for 'clean' liquid-liquid extraction," Chem. Commun. **5**(16), 1765–1766 (1998).
38. H. L. Ngo, K. LeCompte, L. Hargens, *et al.*, "Thermal properties of imidazolium ionic liquids," Thermochim. Acta **357-358**, 97–102 (2000).
39. J. H. Gong, F. Yang, Q. Shao, *et al.*, "Microwave absorption performance of methylimidazolium ionic liquids: towards novel ultra-wideband metamaterial absorbers," Appl. Phys. A **7**(67), 41980–41988 (2017).
40. F. Yang, J. Gong, E. Yang, *et al.*, "Ultrabroadband metamaterial absorbers based on ionic liquids," Appl. Phys. A **125**(2), 149 (2019).
41. X. D. Chen, T. M. Grzegorczyk, Bae-Ian Wu, *et al.*, "Robust method to retrieve the constitutive effective parameters of metamaterials," Phys. Rev. E **70**(1), 016608 (2004).
42. J. D. Wen, Q. Ren, R. Peng, *et al.*, "Multi-functional tunable ultra-broadband water-based metasurface absorber with high reconfigurability," J. Phys. D: Appl. Phys. **55**(28), 285103 (2022).
43. R. Yang, C. Dai, C. Wan, *et al.*, "Planar ultrathin omni-directional perfect absorber utilizing amorphous silicon for photovoltaics," Opt. Mater. Express **10**(2), 532–539 (2020).
44. J. M. Zhang, C. Liu, T. Wang, *et al.*, "Investigating the absorption performance of a monolayer-coated absorber at oblique incidence," J. Phys. D: Appl. Phys. **55**(6), 065001 (2022).
45. Y. H. Liao, S. Zhang, Z. Tang, *et al.*, "Power loss density of electromagnetic waves in unimolecular reactions," RSC Adv. **7**(43), 26546–26550 (2017).
46. A. P. Pancheha, A.A. Puzenko, S.A. Puzenko, *et al.*, "Boundary-conditions for the electromagnetic-field on a non-differentiable fractal surface," Phys. Lett. A **182**(4-6), 407–410 (1993).
47. Z. Wu, X. Chen, Z. Zhang, *et al.*, "Design and optimization of a flexible water-based microwave absorbing metamaterial," Appl. Phys. Express **12**(5), 057003 (2019).
48. L. Wang, X. Yu, X. Li, *et al.*, "MOF-derived yolk-shell Ni@C@ZnO Schottky contact structure for enhanced microwave absorption," Chem. Eng. J. **383**, 123099 (2020).
49. M. Qin, L. Zhang, H. Wu, *et al.*, "Dielectric loss mechanism in electromagnetic wave absorbing materials," Adv. Sci. **9**(10), 9 (2022).